


Modeling of optical binding of submicron aerosol particles in counterpropagating Bessel beams

Journal Article**Author(s):**

Thanopoulos, Ioannis; Luckhaus, David; Signorell, Ruth 

Publication date:

2017-06

Permanent link:

<https://doi.org/10.3929/ethz-b-000190873>

Rights / license:

[In Copyright - Non-Commercial Use Permitted](#)

Originally published in:

Physical Review A 95(6), <https://doi.org/10.1103/PhysRevA.95.063813>

Funding acknowledgement:

172472 - Phase Transitions of Ultrafine Aerosol Particles: Condensation, Freezing, and Metal Formation in Confined Systems (SNF)

Modeling of optical binding of submicron aerosol particles in counterpropagating Bessel beamsI. Thanopoulos,^{1,2,*} D. Luckhaus,^{3,†} and R. Signorell^{3,‡}¹*Department of Optics and Optometry, T.E.I. of Western Greece, Aigio 25100, Greece*²*Theoretical Physical Chemistry Institute, National Hellenic Research Foundation, Athens 11635, Greece*³*Laboratory of Physical Chemistry, Vladimir-Prelog-Weg 2, ETH Zurich, CH-8093 Zurich, Switzerland*

(Received 22 December 2016; published 13 June 2017)

We theoretically investigate the interparticle force between a pair of spherical aerosol nanoparticles in a dual counterpropagating Bessel beam configuration. We study the dependence of optical binding in the aerosol phase on the wavelength of the electromagnetic radiation, the particle radius, and the refractive index, including the cases of weak, moderate, and strong light absorption by the particles. We also investigate the relation between optical binding and the time-averaged intensity of the incident and scattered light. Our results show that optical binding in the aerosol phase depends strongly on the specific values of these parameters. This explains some of the difficulties associated with optical binding experiments with aerosol nanoparticles.

DOI: [10.1103/PhysRevA.95.063813](https://doi.org/10.1103/PhysRevA.95.063813)**I. INTRODUCTION**

The momentum of light and the exertion of optical forces has been at the core of major advances in the research of atomic to microparticle systems over the past few decades. Laser cooling [1] and Bose-Einstein condensation [2] are the primary examples for atomic systems, while the mechanical effects of light have also been exploited in larger systems, for example through the controlled motion or trapping of microscopic particles by light with no physical contact or damage whatsoever [3,4]. This ability to move colloidal particles at will has led to important advances in biological sciences [5], and also other areas, where studies of the laws of thermodynamics [6,7] and Brownian dynamics at the microscopic level [8], optical angular momentum transfer [9,10], and microrheology of particles [11,12] have benefited from the targeted application of optical forces.

Optical forces on particles arise from the change of their momentum due to the interaction with the incident light. They are often classified into scattering and gradient forces [3]. Scattering forces arise from temporal changes in light momentum upon the scattering from an object and point in the direction of propagation of the light [13]. Gradient forces occur whenever spatial intensity [5] or phase gradients [14] are present. For small objects, with sizes much smaller than the wavelength, they are described by the interaction of an induced dipole with the spatial field gradient of the focused electromagnetic radiation. For particles much larger than the wavelength of the light, and with a refractive index exceeding that of the surroundings the refraction of light causes the particle to be pulled towards the maximum field intensity. In general, a proper treatment requires the calculation of optical forces by Maxwell's stress tensor [15]. The increased interest in optical forces arises from the fact that optical scattering forces have properties that differ from electrostatic forces, e.g., they are not conservative [14] and can result in nonreciprocal interactions between constituents [16].

A peculiar manifestation of optical forces is the phenomenon of optical binding [13,15], which can be realized, for example, in dual counterpropagating (CP) beam configurations. In addition to the forces from the incident beams, the binding forces rely on the modification of the incident electromagnetic fields, primarily through interference, by the presence of multiple simultaneously illuminated objects. The phenomenon of optical binding comprises both attractive and repulsive forces. More precisely, under “optical binding” one can understand the mechanism based on light-mediated momentum exchange between particles leading to spatial configurations of particles or clusters of particles with distances between them larger than the extent of any electrostatic forces from any surface charge distributions present [15].

Initially more of a side topic in the field of optical trapping and manipulation [17–20], optical binding has become a rich research area of its own. After first demonstrations [17,18], increased interest in optical binding forces has arisen due to the fact that it features some very interesting physics, including optical force measurement in liquids [21], optical binding in air [22,23] and liquids [24], optical binding of aerosols in white light [25], optical binding of cells *in vivo* [26], evanescent field optical binding in solution [27–29], angular optical binding of colloids [30], broadband transverse optical binding in vacuum [31], and optical binding in standing waves in water [32,33]. We also note that theoretical work has been published on deriving optical binding and its properties from quantum electrodynamics [34–37]; however, such first-principle studies so far can only provide an approximate description of two particles in a laser field, still relatively far away from a realistic simulation of submicron particles in laser beams corresponding to realistic experimental configurations.

Moreover, optical scattering forces have a complex dependence on the interparticle distance, so that optical binding can hardly be predetermined by the spatial shaping of the incident beam, in contrast to the case of single or multiple beam optical trapping [15].

Manifestation of optical binding in systems in the condensed phase has attracted a considerable amount of experimental and theoretical work [17,18,21,24,27–29,32,33,38–41], while work on optical binding of aerosol systems is sparse [22,23,25,31]. A main reason for this is that optical binding in

*ithano@eie.gr

†david.luckhaus@phys.chem.ethz.ch

‡rsignorell@ethz.ch

solutions can be more easily studied experimentally, as well as theoretically. In experiments, optical binding in condensed phase is easier to observe than in air as particle diffusion is much slower; in addition, for the same reason, optical binding in liquids is more robust, i.e., much less sensitive to small parameter changes, than in air. In theory, the small contrast between the refractive index of the particles with respect to the refractive index of the medium makes calculations of optical forces on particles in liquids less computationally demanding than in vacuum; nevertheless, most theoretical work on optical binding in liquids uses approximative methods, instead of solving the exact Maxwell's equations for the matter-light system.

Unfortunately, work on optical binding in the condensed phase is of very limited value for optical binding of aerosol systems due to the nonrepresentative small contrast of the particle-medium refractive index, as well as the approximative methodologies used. Moreover, there is very little work in the literature on how various parameters, such as the size and refractive index of the two particles, and the wavelength and intensity of the illuminating light, affect the possibility of optical binding in the condensed phase. It is thus not surprising that practically nothing is known on this subject for aerosol particle pairs. With the increasing interest in optical binding, we believe that it is high time for such a study; even more so in hindsight as our investigation of these parameters with respect to optical binding in submicron aerosol particles clearly shows that in such a case optical binding exists as a fine balance between those parameters.

In this work we systematically investigate the properties of longitudinal optical binding of a pair of dielectric nanoparticles in air in the geometry of two counterpropagating Bessel beams (CPBB) [42], with respect to the wavelength of the electromagnetic radiation, the size of the particle, and its complex index of refraction.

This paper is organized as follows. Section II briefly presents our methodology for modeling optical binding between spherical particles in a dual CPBB configuration. In Sec. III, we discuss the dependence of optical binding on the size of two dielectric nanoparticles in such a geometry. We further investigate the interrelation of particle radius, wavelength, and the real part of the index of refraction in controlling the optical binding of a pair of identical (nonabsorbing) nanoparticles in a dual CPBB geometry in Sec. IV. In Sec. V we consider the dependence of optical binding on the absorption of light and the role of the light intensity. We conclude in Sec. VI.

II. MODELING OPTICAL BINDING IN A CPBB

In this work, we study the optical forces between submicron particles (200–700 nm) of spherical shape (radius r) in a configuration of two CPBBs in air (refractive index equal 1). Exploiting their “nondiffractive” properties, Bessel beams (BBs) have been used for trapping and guiding of aerosol particles (for a detailed discussion, see Ref. [42] and references therein). In a previous study we investigated the possibility of optical binding of two dielectric submicron particles in the geometry of two CPBBs with a relative polarization angle of 90° [42]. Here we further study the dependence of optical

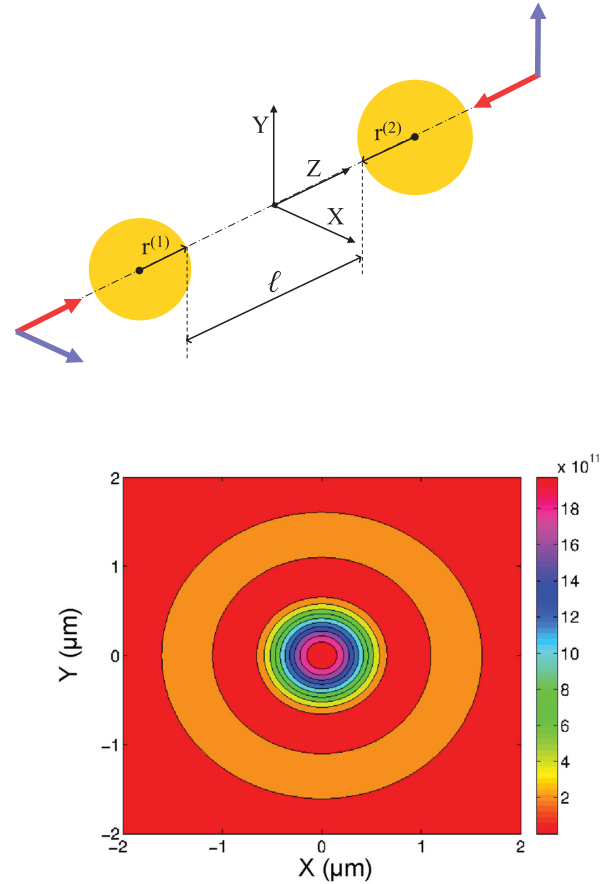


FIG. 1. Top: sketch of the geometrical arrangement of BBs and particles. For each BB the direction of propagation is indicated by the red arrow and the direction of polarization by the blue arrow. $r^{(i)}$ is the radius of particle i and ℓ is the distance between the two particle surfaces. The origin lies at the midpoint between the two particle surfaces so that the center of particle (1) is located at $Z = -\ell/2 - r^{(1)}$ and that of particle (2) at $Z = \ell/2 + r^{(2)}$. Bottom: calculated electric-field intensity (in V^2m^{-2}) profile of an individual zeroth-order BB as used in the present work. The corresponding wavelength is 532 nm.

binding of such particles in a CPBBs configuration on the radii of the particles, the wavelength of the light, and the complex refractive index of the particle.

A. CPBB configuration

The geometrical arrangement of a particle pair in the CPBB configuration is illustrated in the upper panel of Fig. 1, with X, Y, Z standing for the Cartesian axes of the laboratory frame. Each individual BB is assumed to be an ideal linearly polarized pseudo-diffraction-free zeroth-order Bessel beam in its own beam-fixed Cartesian axis system ($\hat{x}, \hat{y}, \hat{z}$). The definition of the electric (\vec{E}) and magnetic (\vec{H}) field components of a x -polarized BB traveling along the z direction as function of the position $\vec{r} = (x, y, z)$ in the beam frame is given in Appendix A. Both particles are located on the axis of propagation of the two BBs (propagating forward and backward, respectively), which we define as the Z axis of the laboratory frame.

We define the orientation of each individual BB in space by a rotation (\mathbf{M}) followed by a translation ($d\vec{r}$) of the

beam-fixed Cartesian axis system $(\hat{x}, \hat{y}, \hat{z})$ with respect to a laboratory-fixed Cartesian axis system $(\hat{X}, \hat{Y}, \hat{Z})$. Both are right handed. The beam-fixed axes are tied to the directions of polarization (\hat{x}) and propagation (\hat{z}) with the origin at the point of maximum intensity, i.e., the center of the beam at half of the diffraction-free propagation distance of the BB (see Appendix A for a detailed discussion). The transformation of laboratory-fixed coordinates $\vec{R} = (X, Y, Z)$ to beam-fixed coordinates $\vec{r} = (x, y, z)$ is given in Appendix A. With this definition, the fields arising from multiple BBs are first calculated individually (\vec{E}_b, \vec{H}_b) in their respective beam-fixed systems, followed by the rotation back to the laboratory-fixed system, and finally added up to yield the total fields \vec{E}_{tot} and \vec{H}_{tot} (discussed in detail in Appendix A).

The BB parameters used in our calculations are given in Appendix A. In the lower panel of Fig. 1, the calculated electric-field intensity $I(x, y, 0) \equiv |\vec{E}(x, y, z)|^2$ (in V^2m^{-2}) profile of a single zeroth-order BB used as in the present work is shown. The corresponding wavelength is 532 nm. The typical bright, circular core surrounded by concentric rings of approximately the same power is visible. Note that the power in the core is about 7 mW and about 9 mW in each of the rings.

B. Optical forces

We calculate the optical force \vec{F} acting on a particle by integrating Maxwell's stress tensor $\hat{\mathbf{T}}$ over the (closed) surface S of the particle [43],

$$\vec{F} = \left\langle \oint_S \hat{\mathbf{T}} \cdot \hat{\mathbf{n}} dS \right\rangle_t, \quad (1)$$

with

$$\hat{\mathbf{T}} = \epsilon_0 \vec{E} \otimes \vec{E} + \mu_0 \vec{H} \otimes \vec{H} - q(\hat{X} \otimes \hat{X} + \hat{Y} \otimes \hat{Y} + \hat{Z} \otimes \hat{Z}), \quad (2)$$

where $q \equiv (\epsilon_0 E^2 + \mu_0 H^2)/2$, \otimes denotes the dyadic product, $\hat{\mathbf{n}}$ stands for the unit vector normal to dS , and $\hat{X}, \hat{Y}, \hat{Z}$ stand for the Cartesian unit vectors of the laboratory frame. The $\langle \dots \rangle_t$ symbol denotes time averaging over the duration of the particle illumination.

We solve Eqs. (1) and (2) with the finite-difference time domain (FDTD) method [44,45] as implemented in the FDTD Solutions package [46] under the assumption of perfect coherence between the two CPBBs, i.e., we use the total fields \vec{E}_{tot} and \vec{H}_{tot} in Eq. (2), obtained as discussed above. The FDTD approach is exact, but also becomes numerically very demanding as the particle size increases. To converge the forces to better than 1%, a particle with a radius comparable to the wavelength λ in the Bessel beam specified above required simulation boxes extending for more than $\pm 40\lambda$ in the transverse directions and a grid finesse significantly better than $\lambda/100$ close to the particle. The solution of the FDTD equations on grids of such size ($> 10^8$ cells including absorbing boundaries) typically took 10 h on 64 processors (AMD Opteron 6174) sharing 64 GB of memory. If not otherwise stated, we expect all FDTD results quoted in this work to be accurate within a few percent. We note that the significant computational expense of FDTD calculations is a

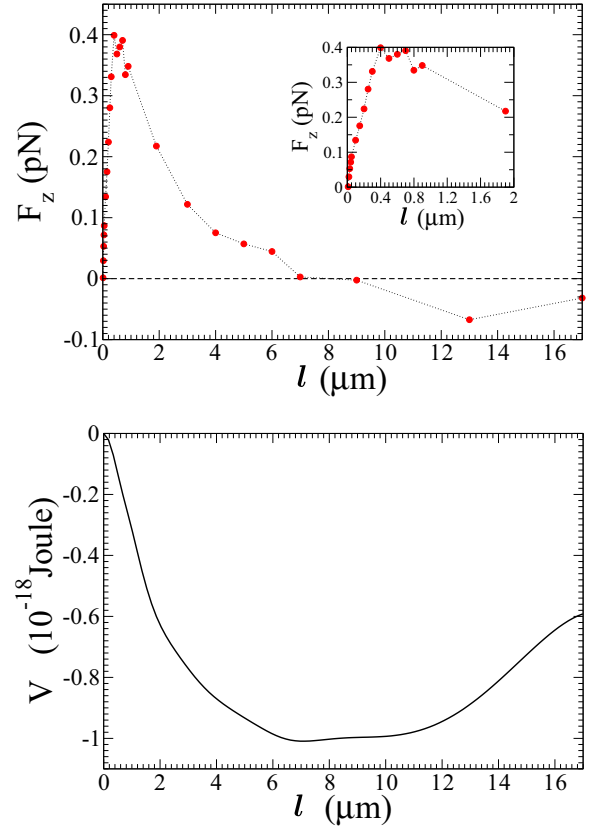


FIG. 2. Interparticle force $F_z(\ell)$ (top panel) and the optical binding potential $V(\ell)$ (bottom panel) for a pair of two identical particles as a function of the distance ℓ between the two particle surfaces. The particles have a radius of 250 nm and are nonabsorbing with an index of refraction $n = 1.42$.

serious limiting factor on the density of calculated points for each case investigated below.

III. DEPENDENCE OF OPTICAL BINDING ON PARTICLE SIZE

A. Optical binding of a symmetric particle pair

We first consider two identical nonabsorbing spherical particles. The wavelength of light is $\lambda = 532$ nm and the refractive index equals $n = 1.42$. We note that for spheres with $n = 1.42$ and radii between 250 and 400 nm, no pronounced Mie resonances occur in the wavelength range between 450 and 600 nm. The corresponding scattering cross sections as a function of λ are slowly varying, almost flat, curves (not shown here). Therefore, we expect that the results obtained with $\lambda = 532$ nm are typical for the above wavelength range.

In the top panel of Fig. 2, we show the interparticle force between two spherical nonabsorbing particles, $F_z(\ell) = (F_z^{(2)} - F_z^{(1)})/2$, of radius $r = 250$ nm as a function of the interparticle distance ℓ between the two particle surfaces. $F_z^{(i)}$ is the force on particle i (see Fig. 1). $F_z > 0$ corresponds to particle repulsion and $F_z < 0$ to particle attraction. $F_z(\ell) = 0$ corresponds to a stationary point with $dF_z(\ell)/d\ell < 0$ for a stable equilibrium position and $dF_z(\ell)/d\ell > 0$ for a barrier.

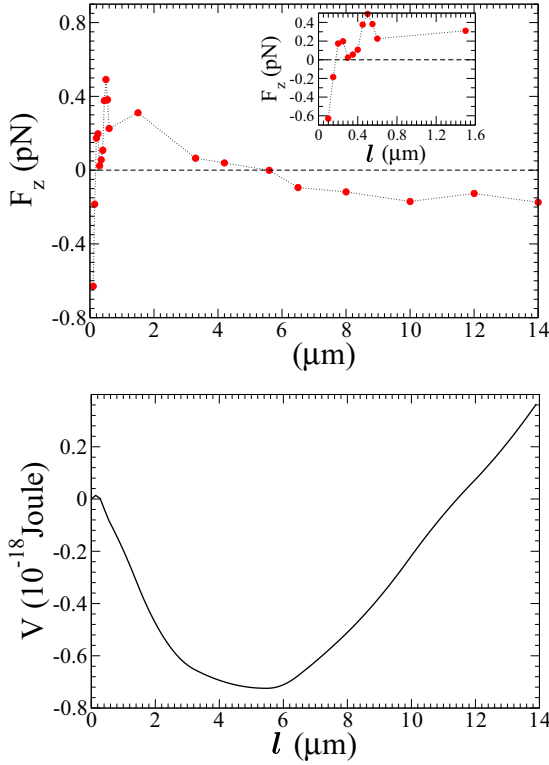


FIG. 3. Interparticle force $F_z(\ell)$ (top panel) as function of the distance of the two particle surfaces ℓ (the inset focuses on $\ell < 1.6$ microns) and the optical binding potential $V(\ell)$ (bottom panel) for a pair of two identical nonabsorbing spherical particles with $n = 1.42$ and $r = 300$ nm.

For this particle pair, the equilibrium position lies at about 7 microns (Fig. 2). At shorter distances, the particles repel each other with maximum repulsion in the range $\ell \approx 400$ –800 nm. The repulsion between the two particles vanishes as ℓ approaches zero, which implies that particles with sufficient kinetic energy can eventually coalesce. The energy required for coalescence can be estimated from the optical binding pair potential, $V(\ell)$, given by

$$V(\ell) = - \int_0^\ell F_z(x) dx, \quad \text{with } V(0) = 0. \quad (3)$$

For the pair of identical nonabsorbing particles ($r = 250$ nm; $n = 1.42$) the result is shown in the bottom panel of Fig. 2. The interparticle equilibrium distance for optical binding, at $\ell \approx 7$ microns, is the distance corresponding to the bottom of the potential well. The potential difference from the equilibrium position to the position of $\ell = 0$ is about ≈ 1 aJ. This energy is the (minimal) kinetic energy for the particle pair to coalesce, which for a particle of this size, and with a typical density of 1.1 g/cm^3 , corresponds to a velocity of ≈ 17 cm/s.

In Fig. 3, we show the interparticle force $F_z(\ell)$ and potential $V(\ell)$, in the top and bottom panel, respectively, for a pair of identical nonabsorbing particles with a radius of 300 nm, again with $n = 1.42$ at $\lambda = 523$ nm. The equilibrium distance is ≈ 5.5 microns, shorter than for 250 nm particles; in addition, a barrier exists at about 200 nm. The binding force $F_z(\ell)$ becomes attractive, at very short interparticle

distances, $\ell \leq 200$ nm (Fig. 3, left). Therefore, coagulation of the two particles is possible, and more facile than for a pair of particles with 250 nm radius. The minimal kinetic energy for coalescence of such a particle pair is a little less than in the case of particles with 250 nm radius, estimated to be ≈ 0.75 aJ. For a particle with 300 nm radius, and with a typical density of 1.1 g/cm^3 , this corresponds to a velocity of ≈ 11 cm/s.

The particle velocities of 10–20 cm/s required for coalescence in the above cases are much larger than particle velocities occurring in typical experiments. For larger radii $r \geq 350$ nm, however, the optical interparticle force between identical nonabsorbing particles ($n = 1.42$ at $\lambda = 532$ nm), turns out to be always attractive [42]; thus no optical binding is possible in those cases and particles would readily coalesce.

We note that in general dispersion forces between the two spherical particles are always, i.e., in free space or under irradiation, present [47]. These forces are attractive between the two particles; moreover, one can estimate [47] that for particles of radius R , the force $F_{\text{disp}}^{\text{max}}(\ell) = \frac{A}{24\pi} \left(\frac{R^2}{\ell^3}\right)$ is an upper bound for the corresponding dispersion forces, where A stands for the Hamaker constant [47], a material characteristic constant, and ℓ is the distance between the particles. [$F_{\text{disp}}^{\text{max}}(\ell)$ is obtained as the dispersion force between two parallel circular disks of radius R at distance ℓ .] For dielectric materials, the Hamaker constants do not exceed $10^2 \times 10^{-20} \text{ J}$ [47]. Therefore, the corresponding forces are several orders of magnitude smaller than the optical forces between the particles under the conditions discussed here. The dynamics of the two particles is thus characterized predominantly by the features of the optical binding forces.

B. Optical binding of an asymmetric particle pair

We now focus on a pair of spheres of different size (radius $r^{(1)}$ and $r^{(2)}$, respectively), again with refractive index $n = 1.42$ at $\lambda = 532$ nm. We compute the interparticle force, as a function of the distance between the two particle surfaces ℓ , for pairs with particle radii of $r^{(1)} = 250, 300, 350$ nm and $200 \leq r^{(2)} \leq 700$ nm.

In Fig. 4, we present contour plots of the interparticle force $F_z(\ell)$ in pN, for particle pairs with $r^{(1)} = 250$ nm (top panel), $r^{(1)} = 300$ nm (middle panel), and $r^{(1)} = 350$ nm (bottom panel), as a function of $r^{(2)}$ ($200 \leq r^{(2)} \leq 700$ nm), and the interparticle distance ℓ . We find optical binding for pairs with particle radii $r^{(2)}$ in the range ≈ 200 –400 nm. The optical binding equilibrium distance, i.e., the value of ℓ where the optical force changes from negative to positive, varies between 0.5 and 6.5 microns for pairs with at least one particle with a radius larger than 250 nm. When both particles have radii smaller than 250 nm, the equilibrium distance can even exceed 9 microns. In all three panels of Fig. 4 we observe the general trend that the magnitude of attractive interparticle forces [$F_z(\ell) < 0$] increases with increasing difference in size between the two spheres, up to 3.5 pN in absolute value. By contrast, repulsive interparticle forces [$F_z(\ell) > 0$], which occur for small differences between the two particle radii, are always less than 0.5 pN in magnitude.

We note that the contour plots in Fig. 4 are obtained by two-dimensional linear interpolation of the calculated $F_z(r^{(2)}, \ell)$

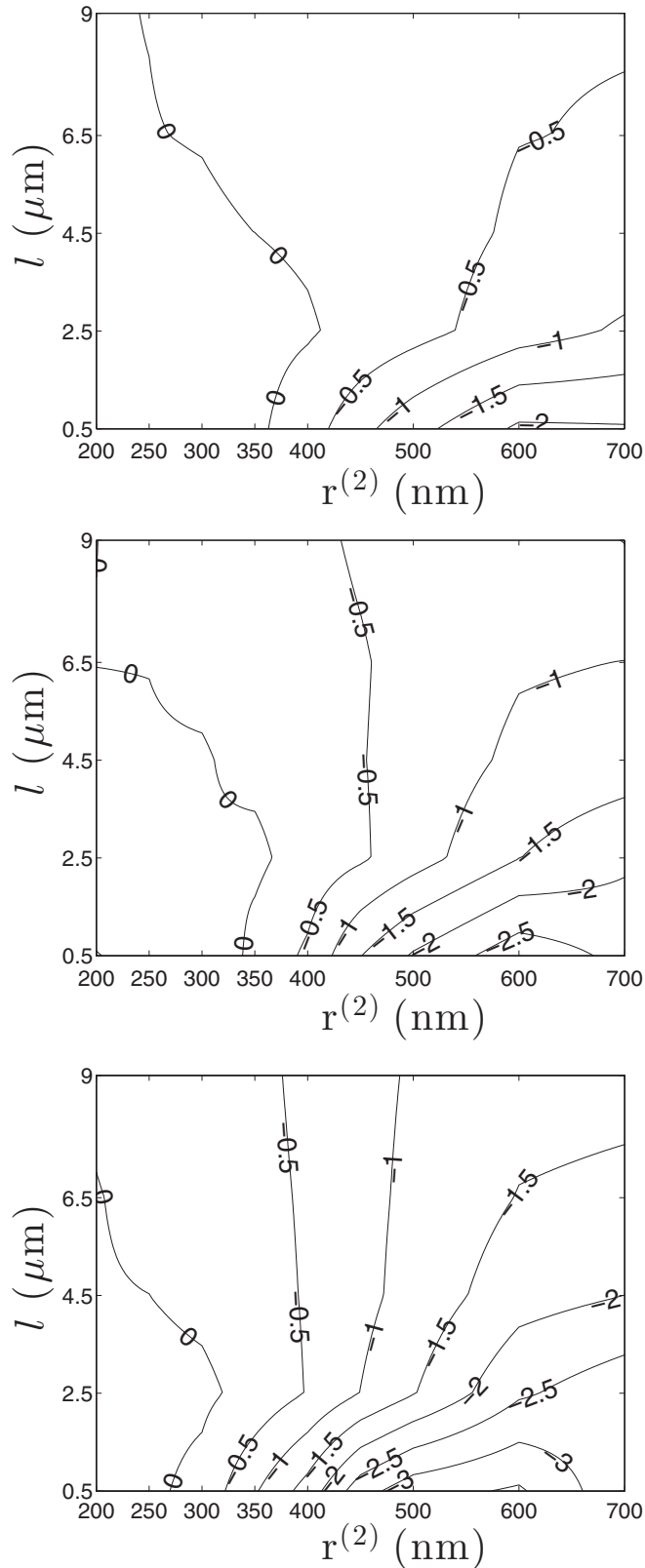


FIG. 4. Contour plots of the interparticle force $F_z(\ell)$ (in pN) as function of the distance ℓ between the two particle surfaces, and the radius of the second particle $r^{(2)}$, for first particle radius $r^{(1)} = 250$ nm (top panel), $r^{(1)} = 300$ nm (middle panel), and $r^{(1)} = 350$ nm (bottom panel). The refractive index is $n = 1.42$ and $\lambda = 532$ nm.

given in Tables I–III in Appendix B. The sharp features in the contour lines only arise from the finite numerical resolution and have no physical meaning. We refrain from using nonlinear interpolation methods for smoothing out these discontinuities because such methods introduce artifacts in the contour plot representation arising from the nonlinear interpolation method used.

IV. DEPENDENCE OF OPTICAL BINDING ON WAVELENGTH AND REAL REFRACTIVE INDEX

The particle radius r , its real refractive index n , and the wavelength λ of the trapping light are three basic parameters that influence the optical force on a particle [15]. Two of them also enter in the definition of the size parameter, $2\pi r/\lambda$ (assuming the refractive index of the medium is equal to 1), which is a characteristic quantity in light scattering by a sphere [48]. Many scaling properties remain the same for identical size parameter. Therefore, one might expect that optical binding also shows a certain trend with, for example, the size parameter. In this section, we investigate the optical binding force for a pair of identical particles, regarding the above three parameters. First, we consider cases where two of the above parameters fulfill a certain mathematical relation, i.e., fixed ratios r/λ and λ/n , and fixed product $r \cdot n$. We then investigate the dependence of the optical force on each of the parameters λ and n independently. In this section we only consider nonabsorbing particles. The dependence of optical binding on light absorption is discussed in the next section.

In the top panel of Fig. 5, we present the optical binding force $F_z(\ell)$ for the case of fixed $\lambda/n = 345.4$ nm, for a pair of particles with radius $r = 350$ nm, for $\lambda = 449.09$ nm and $n = 1.3$ (black curve) and $\lambda = 532$ nm and $n = 1.54$ (red curve). In the middle panel of the same figure, we show $F_z(\ell)$ for the case of fixed $r/\lambda = 0.56$, for a pair of particles with $n = 1.42$, for $r = 250$ nm and $\lambda = 449.09$ nm (black curve) and $r = 350$ nm and $\lambda = 625$ nm (red curve). Lastly, in the bottom panel of Fig. 5, we present the case of fixed $r \cdot n = 455$ nm, at wavelength $\lambda = 440.09$ nm, for $r = 250$ nm and $n = 1.82$ (black curve) and $r = 350$ nm and $n = 1.3$ (red curve). The results, in all three cases, clearly demonstrate that the optical binding force of a particle pair can be quantitatively [magnitude of $F_z(\ell)$] and qualitatively [sign of $F_z(\ell)$] different, even when the ratios or product of two parameters out of (λ, r, n) are fixed and the third parameter is the same. In particular, there is no general trend as a function of the size parameter $2\pi r/\lambda$.

We further study the dependence of the interparticle force between a pair of identical particles on the above three parameters without any mathematical relation between them. Here, we only address the dependence on the wavelength of light λ and the particle refractive index n , since the dependence on r has already been discussed in Sec. III above.

In the top panel of Fig. 6, we present the optical binding force $F_z(\ell)$ for different λ for $n = 1.42$. For decreasing wavelength, we observe that the optical binding force becomes gradually more attractive, with similar qualitative features, e.g., the $F_z(\ell)$ curves retain a similar shape as λ changes from 532 nm to 449.09 nm. However, the changes in magnitude of $F_z(\ell)$ do not reflect the magnitude of the change in λ in a quantitative way.

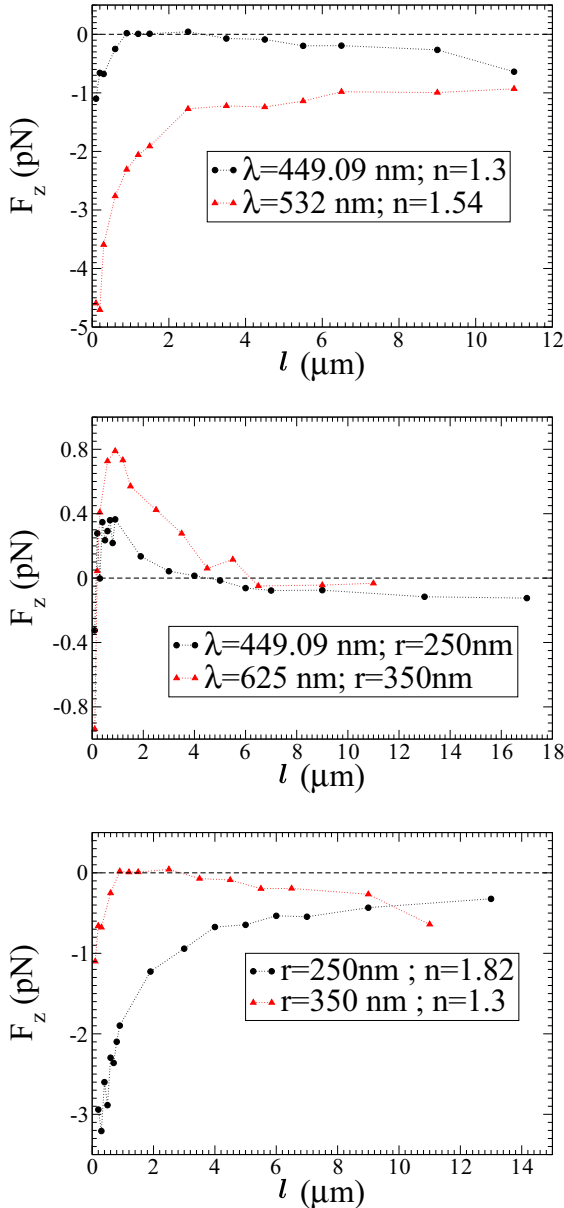


FIG. 5. Optical binding force $F_z(\ell)$ of a pair of identical spherical nonabsorbing particles as function of the distance ℓ between their surfaces, for fixed λ/n and $r = 350$ nm (top panel), fixed r/λ and $n = 1.42$ (middle panel), and fixed $r \cdot n$ and $\lambda = 449.09$ nm (bottom panel). See text for discussion.

The bottom panel of Fig. 6 shows the dependence of $F_z(\ell)$ for a pair of identical particles with real refractive indices n between 1.3 and 1.54, irradiated by light at a fixed wavelength of 487.09 nm. Here, we find that the interparticle force can change qualitatively as the refractive index increases, altering from repulsive to attractive. Moreover, the shape of the $F_z(\ell)$ curves differ qualitatively for different values of n ; while the shape of $F_z(\ell)$ for $n = 1.3$ resembles that for $n = 1.42$, this is not the case for the curve with $n = 1.54$. Note that the relative change in the refractive index from 1.3 to 1.42 and from 1.42 to 1.54 is the same. There is apparently no direct quantitative relationship between the change in the magnitude of $F_z(\ell)$ and the change in the value of n .

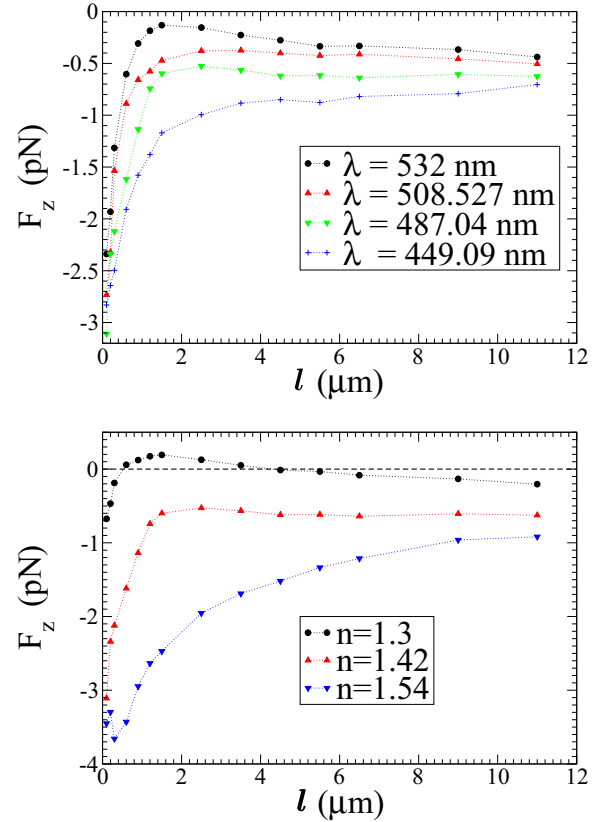


FIG. 6. Optical binding force $F_z(\ell)$ for a pair of identical spherical nonabsorbing particles of 350 nm radius. Top panel: $n = 1.42$ and various values of the wavelength λ . Bottom panel: $\lambda = 487.04$ nm and various values of the refractive index n .

The results shown in Fig. 6 are for a pair of spherical particles with 350 nm radius. We have also studied the case of $r = 250$ nm (not shown here) with similar results as found for the case $r = 350$ nm.

V. OPTICAL BINDING OF ABSORBING PARTICLES

So far, we have neglected the influence of light absorption on optical binding. Here, we address this issue by considering a complex refractive index $n = 1.42 + ik$, with nonvanishing imaginary part k . We neglect photophoresis effects [49] due to the heating of the particles by the absorbed light [50], which is important primarily for optical binding in liquids. We also note that any momentum acquired through the process of photon absorption, in these absorbing systems, would be compensated by the counterpropagating beam geometry.

In Fig. 7, we present the optical binding force $F_z(\ell)$ of a pair of identical spheres for various values of k , ranging from weak absorption, $k = 0.01$, to very strong absorption, $k = 1$. In the top panel of this figure, we show $F_z(\ell)$ for an interparticle distance ℓ of less than one micron. The optical binding force for $\ell > 1$ microns is depicted in the bottom panel of Fig. 7.

The results in Fig. 7 show two qualitatively different aspects of optical binding for absorbing particles. For weak to moderate absorption ($k < 0.1$), we observe that the $F_z(\ell)$ curves are not very different from the $F_z(\ell)$ curve corresponding to nonabsorbing particles. More importantly, weak to moderate

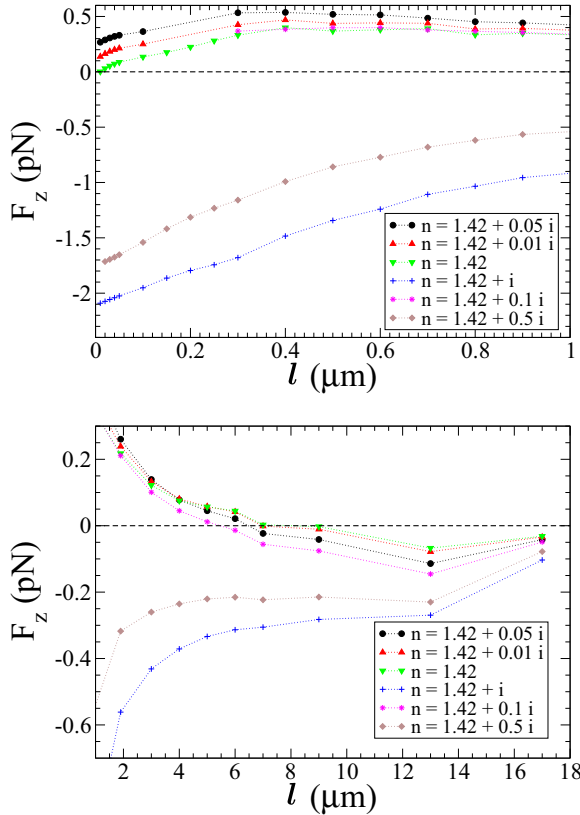


FIG. 7. Optical binding force $F_z(\ell)$, for $\ell < 1$ micron (top panel) and for $\ell > 1$ micron (bottom panel), for a pair of identical absorbing spheres of radius $r = 250$ nm with complex refractive index $n = 1.42 + ik$, as a function of the imaginary part k .

absorption does not necessarily lead to a reduction of repulsive forces, contrary to what one might expect, based on the argument that when the intensity of light in between the particles is reduced by absorption (“shadowing”), the light pressure on each particle will dominate, resulting in enhanced attraction between the particles. The fact that this is not the case is a strong indication that optical binding of particles, even under conditions of moderate light absorption, arises primarily from the interference of the incident and scattered light, and is thus very hard to predict “intuitively.” Only when the light absorption becomes strong, ($k > 0.1$) can enhanced particle attraction be expected, since the light pressure on each particle will dominate; this is confirmed by the results shown in Fig. 7.

The conjecture that optical binding is primarily an interference effect even under conditions of light absorption can be further tested by looking for a relation between the optical interparticle force and the light intensity distribution in between the particle surfaces. For this purpose, we calculate the integrated time-averaged electric-field intensity $\bar{I}(z)$, which is directly proportional to the light intensity along the beam propagation axis z integrated over the other two spatial dimensions:

$$\bar{I}(z) = \frac{1}{T} \int_0^T \int_0^\infty \int_0^\infty |\vec{E}(x, y, z, t)|^2 dx dy dt. \quad (4)$$

T stands for the duration of the irradiation. We consider three cases regarding absorption: (i) no absorption ($k = 0$), (ii) moderate absorption ($k = 0.5$), and (iii) strong absorption ($k =$

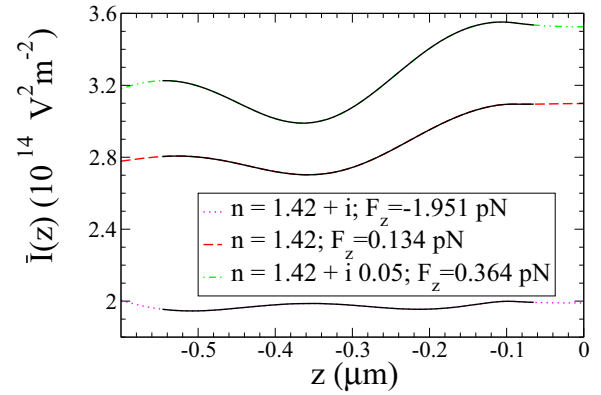


FIG. 8. Integrated time-averaged electric-field intensity $\bar{I}(z)$, along the beam propagation axis z for two spherical absorbing particle of 250 nm radius, located at $z = \pm 0.3$ microns. As the particles are identical $\bar{I}(z)$ is symmetric with respect to $z = 0$. The black part of each curve corresponds to the average intensity inside the particle. See text for discussion.

1). Figure 8 shows the results for two identical particles with a radius of 250 nm located at $z = \pm 0.3$ microns, which yields an interparticle surface distance of $\ell = 100$ nm. For the purpose of investigating the above conjecture it is sufficient to consider $\bar{I}(z)$ in the region $|z| < 0.6$ microns because the optical forces on the particles are completely determined by the Maxwell stress tensor on surfaces just enclosing the respective particle.

Since $\bar{I}(z)$ is symmetric with respect to $z = 0$ for two identical particles, Fig. 8 only shows the results in the region around the particle located at $z = -0.3$ microns. The black part of each curve in Fig. 8 corresponds to the intensity inside the particle. The optical binding force for cases (i)–(iii) is $F_z^{(i)} = 0.134$ pN (repulsion), $F_z^{(ii)} = 0.364$ pN (repulsion), and $F_z^{(iii)} = -1.951$ pN (attraction), respectively. The behavior of $\bar{I}(z)$ for the three cases depicted in this figure indicate that no simple quantitative, nor even qualitative, relation exists between the interparticle force and the intensity of light in the dual CPBB geometry. On the basis of the results for cases (i) and (ii) one might have speculated that repulsion can be observed when $\bar{I}(z)$ is larger in the region in between the particles than on the sides facing the incoming light. Closer inspection of case (iii), however, contradicts such an hypothesis. Here $\bar{I}(z)$ is practically equal on both sides of the particle, while the optical force on this particle is far from vanishing.

In this section, we have investigated a pair of particles of $r = 250$ nm radius. For particles of 300 nm radius similar results were found.

VI. CONCLUSIONS

In this work, we have investigated the optical binding force between a pair of submicron dielectric spherical aerosol particles in a dual CPBB configuration. We have studied particle pairs of the same as well as of different size. We have also investigated the dependence of the optical binding force on the wavelength of the light, the particle radius, and the refractive index, including the cases of weak, moderate, and strong light absorption by the particles. Our results demonstrate the lack of a general systematic relationship between those parameters

and the optical binding force that would allow one to make qualitative predictions on the occurrence of optical binding for a particular dual CPBB configuration. Our calculations do not show any indications for a quantitative relation between optical binding and the light intensity distribution in a dual CPBB configuration. Therefore, we come to the conclusion that there is no intuitively simple way to understand optical binding in a dual CPBB configuration in the aerosol phase. Optical binding of aerosol particles is ultimately based on a fine balance of many parameters making its experimental realization a difficult and treacherous enterprise.

ACKNOWLEDGMENTS

Financial support was provided by the ETH Zürich and the Swiss National Science Foundation (SNF Project No. 200020-172472). The authors also thank support from the COST Action CM1405 (Molim).

APPENDIX A: CALCULATION OF THE $\vec{\mathbf{E}}_{\text{tot}}$ AND $\vec{\mathbf{H}}_{\text{tot}}$ FIELDS IN A MULTIPLE BB CONFIGURATION

The geometrical arrangement of a particle pair in the CPBB configuration is illustrated in the top panel of Fig. 1, with X, Y, Z standing for the Cartesian unit vectors of the laboratory frame. Both particles are located on the axis of propagation of the two BBs (propagating forward and backward, respectively), which we define as the Z axis of the laboratory frame.

All individual BBs are assumed to be ideal linearly polarized pseudo-diffraction-free zeroth-order Bessel beams as defined in Ref. [42]. They result from Gaussian beams (wave number k , waist radius w_c) passing through an axicon with an internal angle δ and a refractive index n_{ax} , which yields a semiapex angle

$$\theta_0 = \arcsin\left(\frac{n_{ax}}{n_0} \sin \delta\right) - \delta. \quad (\text{A1})$$

n_0 is the refractive index of the surrounding medium ($n_0 = 1$ is valid for this work). Such a beam propagates approximately diffraction free over a distance z_{max} starting from the tip of the axicon given by

$$z_{\text{max}} = \frac{w_c}{\tan \theta_0}. \quad (\text{A2})$$

For an x -polarized BB in its own beam-fixed Cartesian axis system $(\hat{\mathbf{x}}, \hat{\mathbf{y}}, \hat{\mathbf{z}})$, traveling along z , the electric- ($\vec{\mathbf{E}}$) and magnetic- ($\vec{\mathbf{H}}$) field components as a function of position $\vec{\mathbf{r}} = (x, y, z)$ are given [42] (we are using SI units throughout):

$$\vec{\mathbf{E}}(x, y, z) = E_0 f(\tilde{z})(E_x \hat{\mathbf{x}} + E_y \hat{\mathbf{y}} + E_z \hat{\mathbf{z}}), \quad (\text{A3})$$

$$\vec{\mathbf{H}}(x, y, z) = \frac{n_0}{c_0 \mu_0} H_0 f(\tilde{z})(H_x \hat{\mathbf{x}} + H_y \hat{\mathbf{y}} + H_z \hat{\mathbf{z}}), \quad (\text{A4})$$

with

$$f(\tilde{z}) = \sqrt{2\tilde{z}} \exp[-\tilde{z}^2 + i\tilde{k}_z \tilde{z} + (1 - i\pi)/4], \quad (\text{A5})$$

$$E_x = J_0(\rho) + \chi^2 J_2(\rho) \cos(2\phi), \quad (\text{A6})$$

$$E_y = \chi^2 J_2(\rho) \sin(2\phi), \quad (\text{A7})$$

$$E_z = -2i J_1(\rho) \cos(\phi), \quad (\text{A8})$$

$$H_x = \chi^2 J_2(\rho) \sin(2\phi), \quad (\text{A9})$$

$$H_y = J_0(\rho) - \chi^2 J_2(\rho) \cos(2\phi), \quad (\text{A10})$$

$$H_z = -2i J_1(\rho) \sin(\phi), \quad (\text{A11})$$

where c_0 is the speed of light in vacuum, μ_0 is the magnetic constant, J_m are Bessel functions of the first kind of order m , $\tilde{k}_z = kz_{\text{max}} \cos \theta_0$, $\chi = \sin \theta_0 / (1 + \cos \theta_0) \rho = k \sin \theta_0 \sqrt{x^2 + y^2}$, $\phi = \arctan(y/x)$, and $\tilde{z} = (z - z_0)/z_{\text{max}}$. The tip of the axicon is located at $\vec{\mathbf{r}} = (0, 0, z_0)$. E_0 is the maximum field amplitude of the beam obtained with a Gaussian beam of power P_T ,

$$E_0 = \left| \vec{\mathbf{E}}\left(0, 0, z_0 + \frac{z_{\text{max}}}{2}\right) \right| = \sqrt{\frac{4P_T k \sin \theta_0}{w_c c_0 \epsilon_0 n_0 \sqrt{e}}}, \quad (\text{A12})$$

where e is Euler's number and ϵ_0 is the electric constant. The core size (r_c) of such a Bessel beam is given by the first zero in radial direction. For $\chi \ll 1$, one obtains

$$r_c \approx \frac{2.4048}{k \sin \theta_0}. \quad (\text{A13})$$

The BB parameters used in our calculations are $P_T = 500$ mW (for each individual beam), $w_c = 0.3$ mm, and $\theta_0 = 6.95$. The resulting core size and propagation length are $r_c = 1.68$ μm and $z_{\text{max}} = 2.46$ mm, respectively.

We further define the orientation of each individual BB in space by a rotation (\mathbf{M}) followed by a translation ($d\vec{\mathbf{r}}$) of a beam-fixed Cartesian axis system $(\hat{\mathbf{x}}, \hat{\mathbf{y}}, \hat{\mathbf{z}})$ with respect to a laboratory-fixed Cartesian axis system $(\hat{\mathbf{X}}, \hat{\mathbf{Y}}, \hat{\mathbf{Z}})$. Both are right handed. The beam-fixed axes are tied to the directions of polarization ($\hat{\mathbf{x}}$) and propagation ($\hat{\mathbf{z}}$) with the origin at the point of maximum intensity (i.e., the center of the beam at a distance $z_{\text{max}}/2$ from the tip of the axicon in the direction of propagation). The transformation of laboratory-fixed coordinates $\vec{\mathbf{R}} = (X, Y, Z)$ to beam-fixed coordinates $\vec{\mathbf{r}} = (x, y, z)$ is given by $\vec{\mathbf{r}} = \mathbf{M}\vec{\mathbf{R}} - d\vec{\mathbf{r}}$. The rotation of the coordinate system is defined in terms of three Euler angles (α, β, γ) for consecutive right-handed rotations: a rotation by α around the Z axis, followed by a rotation by β around the new (intermediate) x' axis, followed by a rotation by γ around the new z axis. The matrix elements $M_{i,j}$ ($i, j = 1, \dots, 3$) of the rotation matrix \mathbf{M} are given by

$$M_{1,1} = \cos \alpha \cos \gamma - \sin \alpha \cos \beta \sin \gamma, \quad (\text{A14})$$

$$M_{1,2} = \sin \alpha \cos \gamma + \cos \alpha \cos \beta \sin \gamma, \quad (\text{A15})$$

$$M_{1,3} = \sin \beta \sin \gamma, \quad (\text{A16})$$

$$M_{2,1} = -\cos \alpha \sin \gamma - \sin \alpha \cos \beta \cos \gamma, \quad (\text{A17})$$

$$M_{2,2} = -\sin \alpha \sin \gamma + \cos \alpha \cos \beta \cos \gamma, \quad (\text{A18})$$

$$M_{2,3} = \sin \beta \cos \gamma, \quad (\text{A19})$$

$$M_{3,1} = \sin \alpha \sin \beta, \quad (\text{A20})$$

$$M_{3,2} = -\cos \alpha \sin \beta, \quad (\text{A21})$$

$$M_{3,3} = \cos \beta. \quad (\text{A22})$$

We note that this is a passive rotation, i.e., $\vec{\mathbf{R}}$ and $\vec{\mathbf{r}}$ are the coordinates of the same vector in two different coordinate systems. The orientation of each of the multiple Bessel beams b (b is the enumerating index for each BB) is defined by the values for $(\alpha_b, \beta_b, \gamma_b)$ and $d\vec{\mathbf{r}}_b = (dx_b, dy_b, dz_b)$.

With this definition, the fields arising from multiple BBs are first calculated individually ($\vec{\mathbf{E}}_b, \vec{\mathbf{H}}_b$) in their respective beam-fixed systems, followed by the rotation back to the laboratory-fixed system, and finally added up to yield the total fields:

$$\vec{\mathbf{E}}_{\text{tot}} = \sum_b \mathbf{M}_b^T \vec{\mathbf{E}}_b (\mathbf{M}_b \vec{\mathbf{R}} - d\vec{\mathbf{r}}_b) \quad (\text{A23})$$

and

$$\vec{\mathbf{H}}_{\text{tot}} = \sum_b \mathbf{M}_b^T \vec{\mathbf{H}}_b (\mathbf{M}_b \vec{\mathbf{R}} - d\vec{\mathbf{r}}_b), \quad (\text{A24})$$

where \mathbf{M}^T stands for the transpose matrix of \mathbf{M} .

TABLE I. Interparticle force $F_z(\ell)$ (in pN) as function of the distance ℓ between the two particle surfaces, and the radius of the second particle $r^{(2)}$, for first particle radius $r^{(1)} = 250$ nm.

$r^{(2)}$ (nm)	ℓ / μ				
	0.5	2.5	4.5	6.5	9
200	0.29945	0.12406	0.03626	0.01226	0.01498
250	0.34557	0.15904	0.04638	0.00616	-0.00341
300	0.33993	0.20098	0.03488	-0.01014	-0.05018
350	0.09298	0.14366	-0.00014	-0.05691	-0.11081
400	-0.26881	0.04325	-0.06027	-0.12270	-0.19848
450	-0.85738	-0.13103	-0.17701	-0.21520	-0.29881
500	-1.32465	-0.32218	-0.28350	-0.32144	-0.37887
600	-2.08964	-0.77321	-0.56879	-0.49056	-0.47920
700	-2.04384	-1.06828	-0.66504	-0.52234	-0.47952

APPENDIX B: DATA USED IN FIG. 5

Tables I–III present the data used in Fig. 5.

TABLE II. Interparticle force $F_z(\ell)$ (in pN) as function of the distance ℓ between the two particle surfaces, and the radius of the second particle $r^{(2)}$, for first particle radius $r^{(1)} = 300$ nm.

$r^{(2)}$ (nm)	ℓ / μ				
	0.5	2.5	4.5	6.5	9
200	0.51879	0.12604	0.05708	-0.00297	0.00129
250	0.33567	0.20650	0.03169	-0.00642	-0.04308
300	0.49177	0.01520	0.03280	-0.08497	-0.13216
350	-0.14811	0.09759	-0.10727	-0.14965	-0.23707
400	-0.58805	-0.19961	-0.21351	-0.32672	-0.39860
450	-1.48683	-0.43172	-0.47883	-0.46041	-0.55956
500	-2.06050	-0.77611	-0.66487	-0.65007	-0.68521
600	-2.81114	-1.49116	-1.11510	-0.94567	-0.85281
700	-2.37096	-1.90908	-1.24847	-1.00870	-0.48531

TABLE III. Interparticle force $F_z(\ell)$ (in pN) as function of the distance ℓ between the two particle surfaces, and the radius of the second particle $r^{(2)}$, for first particle radius $r^{(1)} = 350$ nm.

$r^{(2)}$ (nm)	ℓ / μ				
	0.5	2.5	4.5	6.5	9
200	0.30480	0.17014	0.01443	0.00932	-0.03533
250	0.09663	0.15122	0.00092	-0.05210	-0.10549
300	-0.14994	0.09979	-0.10562	-0.14802	-0.23571
350	-0.95000	-0.15478	-0.27643	-0.33182	-0.36715
400	-1.71182	-0.52686	-0.54794	-0.56796	-0.62181
450	-2.79464	-1.00968	-0.85616	-0.85710	-0.85513
500	-3.30647	-1.47029	-1.18509	-1.11118	-1.04972
600	-3.57203	-2.42372	-1.79757	-1.52081	-1.32125
700	-2.62382	-2.82398	-1.99776	-1.61044	-1.35651

- [1] S. Chu, *Rev. Mod. Phys.* **70**, 685 (1998); C. N. Cohen-Tannoudji, *ibid.* **70**, 707 (1998); W. D. Phillips, *ibid.* **70**, 721 (1998).
- [2] W. Ketterle, *Rev. Mod. Phys.* **74**, 1131 (2002).
- [3] A. Ashkin, *Optical Trapping and Manipulation of Neutral Particles Using Lasers* (World Scientific, London, 2006).
- [4] K. Dholakia and W. M. Lee, *Adv. At. Mol. Phys.* **56**, 261 (2008).
- [5] *Optical Tweezers: Methods and Applications*, edited by M. J. Padgett, J. Molloy, and D. McGloin (Chapman & Hall/CRC Press, Boca Raton, FL, 2010).
- [6] D. M. Carberry, J. C. Reid, G. M. Wang, E. M. Sevick, D. J. Searles, and D. J. Evans, *Phys. Rev. Lett.* **92**, 140601 (2004).
- [7] E. Aurell, K. Gawedzki, C. Mejia-Monasterio, R. Mohayae, and P. Muratore-Ginanneschi, *J. Stat. Phys.* **147**, 487 (2012).
- [8] T. Li, S. Kheifets, D. Medellin, and M. G. Raizen, *Science* **328**, 1673 (2010).
- [9] V. Garcés-Chávez, K. Volke-Sepulveda, S. Chávez-Cerda, W. Sibbett, and K. Dholakia, *Phys. Rev. A* **66**, 063402 (2002).
- [10] K. Toyoda, F. Takahashi, S. Takizawa, Y. Tokizane, K. Miyamoto, R. Morita, and T. Omatsu, *Phys. Rev. Lett.* **110**, 143603 (2013).
- [11] D. Mizuno, D. A. Head, F. C. MacKintosh, and C. F. Schmidt, *Macromolecules* **41**, 7194 (2008).
- [12] R. M. Power, D. R. Burnham, and J. P. Reid, *Appl. Opt.* **53**, 8522 (2014).
- [13] R. W. Bowman and M. J. Padgett, *Rep. Prog. Phys.* **76**, 026401 (2013).
- [14] Y. Roichman, B. Sun, Y. Roichman, J. Amato-Grill, and D. G. Grier, *Phys. Rev. Lett.* **100**, 013602 (2008).
- [15] K. Dholakia and P. Zemanek, *Rev. Mod. Phys.* **82**, 1767 (2010).
- [16] S. Sukhov, A. Shalin, D. Haefner, and A. Dogariu, *Opt. Express* **23**, 247 (2015).
- [17] S. A. Tatarkova, A. E. Carruthers, and K. Dholakia, *Phys. Rev. Lett.* **89**, 283901 (2002).
- [18] V. Karásek, T. Čižmár, O. Brzobohatý, P. Zemánek, V. Garcés-Chávez, and K. Dholakia, *Phys. Rev. Lett.* **101**, 143601 (2008).

- [19] A. E. Carruthers, J. P. Reid, and A. J. Orr-Ewing, *Opt. Express* **18**, 14238 (2010).
- [20] W. Mu, Z. Liu, L. Luan, G. Wang, G. C. Spalding, and J. B. Ketterson, *New J. Phys.* **11**, 103017 (2009).
- [21] N. K. Metzger, R. F. Marchington, M. Mazilu, R. L. Smith, K. Dholakia, and E. M. Wright, *Phys. Rev. Lett.* **98**, 068102 (2007).
- [22] M. Guillon, O. Moine, and B. Stout, *Phys. Rev. Lett.* **96**, 143902 (2006); S. Liu, and J. Yu, *ibid.* **100**, 199403 (2008); M. Guillon, B. Stout, and O. Moine, *ibid.* **100**, 199404 (2008).
- [23] M. Guillon and B. Stout, *Phys. Rev. A* **77**, 023806 (2008).
- [24] O. Brzobohaty, V. Karasek, T. Cizmar, and P. Zemanek, *Appl. Phys. Lett.* **99**, 101105 (2011).
- [25] S. Maayani, L. L. Martin, and T. Carmon, *Opt. Lett.* **40**, 1818 (2015).
- [26] Y. Li, H. Xin, Y. Liu, and B. Li, *Sci. Rep.* **5**, 10925 (2015).
- [27] X. Han and P. H. Jones, *Opt. Lett.* **40**, 4042 (2015).
- [28] M. C. Frawley, I. Gusachenko, V. G. Truong, M. Sergides, and S. Nic Chormaic, *Opt. Express* **22**, 16322 (2014).
- [29] M. D. Summers, R. D. Dear, J. M. Taylor, and G. A. D. Richie, *Opt. Express* **20**, 1001 (2012).
- [30] S. H. Simpson, L. Chvatal, and P. Zemanek, *Phys. Rev. A* **93**, 023842 (2016).
- [31] M. Mazilu, A. Rudhall, E. M. Wright, and K. Dholakia, *J. Phys.: Condens. Matter* **24**, 464117 (2012).
- [32] O. Brzobohatý, T. Čížmár, V. Karásek, M. Šiller, K. Dholakia, and P. Zemánek, *Opt. Express* **18**, 25389 (2010).
- [33] O. Brzobohatý, V. Karásek, M. Šiller, J. Trojek, and P. Zemánek, *Opt. Express* **19**, 19613 (2011).
- [34] J. Rodríguez, L. C. Dávila Romero, and D. L. Andrews, *Phys. Rev. A* **78**, 043805 (2008); J. Rodríguez and D. L. Andrews, *ibid.* **79**, 022106 (2009); **79**, 029902(E) (2009).
- [35] J. Rodríguez, *Opt. Lett.* **33**, 2197 (2008).
- [36] L. D. D. Romero, J. Rodríguez, and D. L. Andrews, *Opt. Commun.* **281**, 865 (2008).
- [37] J. Rodríguez and D. L. Andrews, *Opt. Commun.* **282**, 2267 (2009).
- [38] V. Karasek, O. Brzobohaty, and P. Zemanek, *J. Opt. A: Pure Appl. Opt.* **11**, 034009 (2009).
- [39] Y. Cao, L. Chen, W. Ding, F. Sui, and T. Zhu, *Opt. Commun.* **311**, 332 (2013).
- [40] L. Athanasekos, M. Vasileiadis, C. Matzaridis, V. C. Karoutsos, I. Koutselas, S. Pispas, and N. A. Vainos, *Opt. Express* **20**, 24735 (2014).
- [41] V. Karasek and P. Zemanek, *Proc. SPIE* **8697**, 86970T (2012).
- [42] I. Thanopoulos, D. Luckhaus, T. C. Preston, and R. Signorell, *J. Appl. Phys.* **115**, 154304 (2014).
- [43] J. D. Jackson, *Classical Electrodynamics* (Wiley, New York, 1999).
- [44] A. Taflove and S. C. Hagness, *Computational Electrodynamics* (Artech House, Boston, 2005).
- [45] D. M. Sullivan, *Electromagnetic Simulation Using the FDTD Method* (IEEE Press, Inc., New York, 2000).
- [46] See <http://www.lumerical.com> for FDTD Solutions, Version 8.5.4, Lumerical Solutions, Inc.
- [47] L. Bergstroem, *Adv. Colloid Interface Sci.* **70**, 125 (1997).
- [48] C. F. Bohren and D. R. Huffman, *Absorption and Scattering of Light by Small Particles* (Wiley-Interscience, New York, 1983).
- [49] J. Lin and Y.-Q. Li, *Appl. Phys. Lett.* **104**, 101909 (2014).
- [50] V. G. Shvedov, A. S. Desyatnikov, A. V. Rode, W. Krolikowski, and Y. S. Kivshar, *Opt. Express* **17**, 5743 (2009).